Scripta Materialia 210 (2022) 114413

Contents lists available at ScienceDirect

Scripta Materialia

journal homepage: www.elsevier.com/locate/scriptamat

Sliding energy landscape governs interfacial failure of nanotube-reinforced ceramic nanocomposites

Ning Li[a,1], Christopher M Dmuchowski[b,c,1], Yingchun Jiang[b], Chenglin Yi[b], Feilin Gou[b], Jia Deng[d], Changhong Ke[b,c,**], Huck Beng Chew[a,*]

[a] Department of Aerospace Engineering, University of Illinois at Urbana-Champaign, Urbana, IL 61801, USA
[b] Department of Mechanical Engineering, State University of New York at Binghamton, Binghamton, NY 13902, USA
[c] Materials Science and Engineering Program, State University of New York at Binghamton, Binghamton, NY 13902, USA
[d] Department of Systems Science and Industrial Engineering, State University of New York at Binghamton, Binghamton, NY 13902, USA

ARTICLE INFO

Article history:
Received 16 August 2021
Revised 8 October 2021
Accepted 5 November 2021

Keywords:
Silica-2D material interfaces
Interfacial shear
Sliding energy landscape
Single-nanotube pullout experiments
Density functional theory

ABSTRACT

We report the sliding adhesion of hexagonal boron nitride (hBN) and graphene on silica using single nanotube pullout force measurements and potential energy landscape calculations by density functional theory (DFT). In contrast to isotropic sliding of graphene on silica, the sliding of hBN on silica exhibits strong directional dependence with unusually high energy barriers formed by stacking of unterminated Si or O atoms on N atoms. Stronger interfacial adhesion energy and shear strength across possible termination structures of silica with hBN versus graphene cumulate in the measured interfacial shear strength of ~34.7 MPa versus ~19.2 MPa for the respective nanotube-reinforced composites

Two-dimensional atomic sheets, such as graphene and hexagonal Boron Nitride (hBN), possess large surface areas and surface energies, and tend to interact with the underlying substrate. The shear adhesion properties of single atomic sheets with silica are of particular interest, since this is a common material system used for fundamental property measurements and is technologically relevant to nanodevices and nanocomposites. To-date, wide-ranging interfacial shear strength values of $\sim 2-60$ MPa for mono- or few-layer graphene on silica have been inferred from bulge and pressure blister tests [1,2] or from tribological studies with an atomic force microscope (AFM) probe tip [3]. The reactivity between graphene and silica has also been a source of debate, with some density functional theory (DFT) calculations predicting strong interfacial adhesion [4,5], which contracts experiments [6,7], while others suggesting sensitivity of the interaction to different SiO_2 surfaces [8,9] or the presence of moisture along the interface [10]. Composite studies on the reinforcement of hBN, graphene, and their 1D counterparts – boron nitride nanotubes (BNNTs) and carbon nanotubes (CNTs) – in brittle ceramic matrices are equally conflicting, with toughening mechanisms ranging from nanotube pullout suggesting interfacial failure, to matrix cracking indicative of strongly-bonded interfaces [11–13].

Here, we report the first comparison study of the interfacial shear strength properties of graphene and hBN on silica, measured directly from the pullout of individual CNTs and BNNTs from amorphous silica matrices along with companion DFT calculations. The measured interfacial shear strength (IFSS) for hBN-silica is 45% higher than for graphene-silica. This stronger binding is associated with the anisotropic potential energy landscape, with higher barrier energies for sliding of hBN on silica versus the isotropic, non-directional sliding of graphene on silica. The binding of graphene and hBN with silica transitions from weak physisorption to strong chemisorption depending on the extent of uncoordinated O atoms on the silica surface, which explains the conflicting interfacial shear properties aforementioned.

Our *in situ* scanning electron microscopy (SEM) nanomechanical single-nanotube pullout technique is illustrated in Fig. 1a [14]. In this testing scheme, individual nanotubes are sandwiched between two layers of amorphous silica films. A pre-calibrated AFM cantilever that is mounted to a 3D piezo-stage as a force sensor is controlled to stretch a nanotube out of the silica films by gripping the nanotube's protruding end (Fig. 1b; see *Experimental Methods* in the Supplementary Materials). Double-walled CNTs synthesized using chemical vapor deposition (CVD) methods were

* Corresponding author.
** Corresponding author at: Department of Mechanical Engineering, State University of New York at Binghamton, Binghamton, NY 13902, USA
E-mail addresses: cke@binghamton.edu (C. Ke), hbchew@illinois.edu (H.B. Chew).
[1] These authors contributed equally to this work

https://doi.org/10.1016/j.scriptamat.2021.114413
1359-6462/

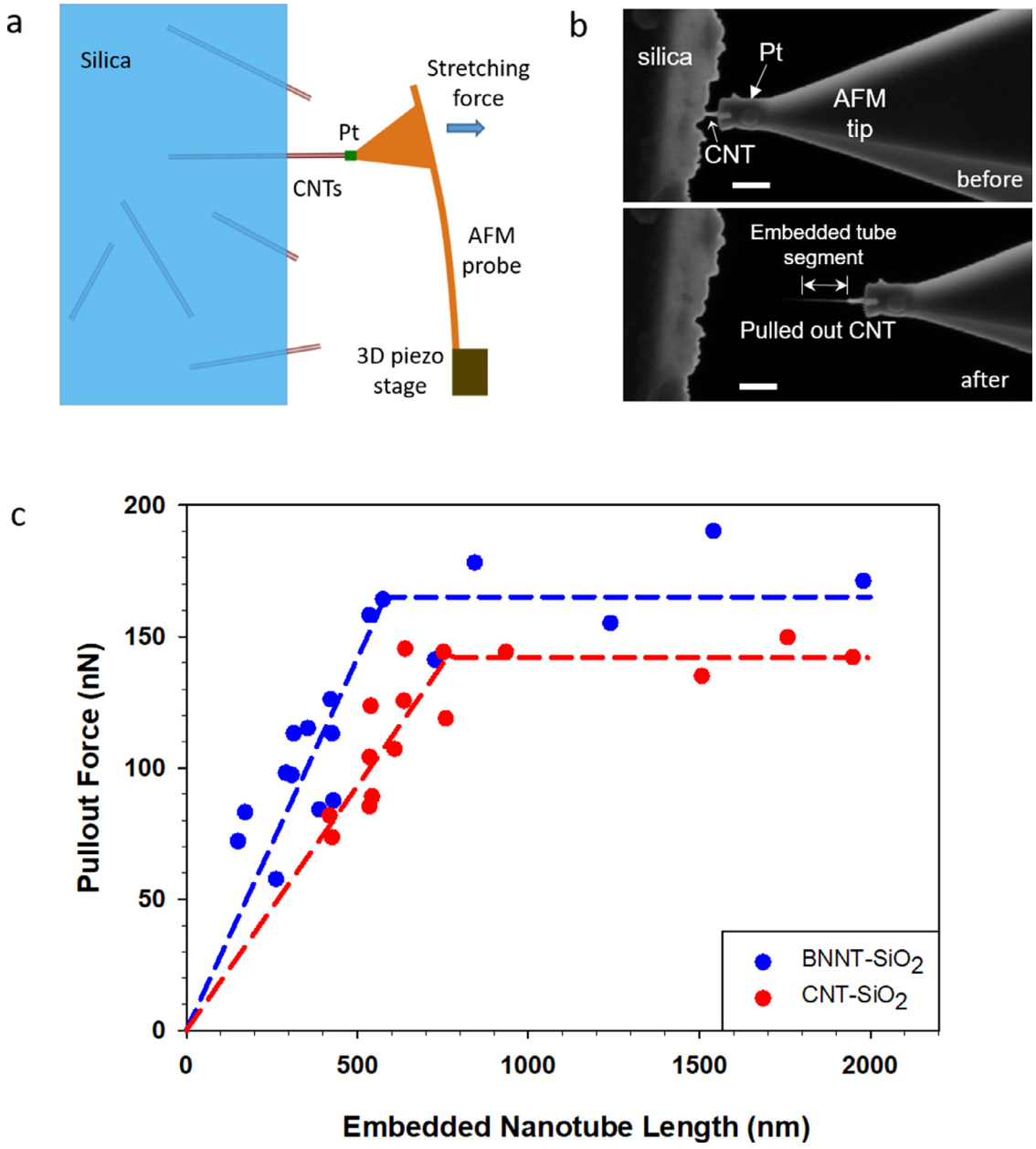

Fig. 1. (**a**) Schematic of *in situ* single-nanotube pullout techniques inside a high resolution SEM. (**b**) Selected SEM snapshots of one typical single nanotube pullout experiment (scale bars 500 nm). The measured pullout force is ~110 nN and the embedded nanotube length is ~600 nm. (**c**) The dependence of the measured pullout force on the embedded nanotube length for CNT-silica and BNNT-silica interfaces. The dashed lines are the bilinear fitting curves. The data for BNNT-silica interfaces are reproduced from [15] (For interpretation of the references to color in this figure, the reader is referred to the web version of this article.).

employed in this study. The small peak intensity ratio of their Raman D and G bands (Fig. S2b in the Supplementary Materials) indicates a low defect level in the nanotubes. In addition to successful nanotube pullout, we also observe two other failure scenarios, namely, nanotube fracture and telescopic pullout, during the nanomechanical measurements (Fig. S3 in the Supplementary Materials). Fig. 1c shows the dependence of the measured pullout force versus the embedded nanotube length based on 15 different successful nanotube pullout experiments (red dots), which displays a bilinear shear-lag behavior. The pullout force linearly increases with embedded nanotube length, but saturates at ~142 ± 3 nN. Included in Fig. 1c is our recent nanotube pullout data on comparable BNNT-silica interface by using the same nanomechanical testing scheme (blue dots) [15]. The pullout force curve obtained for BNNT-silica interfaces displays a similar bilinear trend with a plateau force of ~165 nN. By accounting for the difference in the median nanotube diameter (2.9 nm for BNNTs versus 3.1 nm for CNTs), our nanomechanical measurements reveal that the maximum load carrying capacity of the BNNT-silica interface is, on average, ~24.2% higher than that of the CNT-silica interface on a per unit area basis. The much stronger BNNT-silica interface is also indicated by the steeper slope of the initial increasing segment of the pullout force curve, which is used to calculate the average IFSS (= pullout force/embedded nanotube surface area). We obtain an average IFSS of ~34.7 ± 8.2 MPa for the BNNT-silica interface versus ~19.2 ± 1.5 MPa for the CNT-silica interface based on the nanotubes' median diameters. These IFSS values for CNT-silica are significantly higher than the ~2 MPa interfacial shear stresses inferred from bulge and pressure blister tests for graphene on silica [1,2], but are lower than the ~60 MPa interfacial shear strength

measured from tribological studies using AFM [3], and are comparable to the IFSS values (10–33 MPa) obtained from single-fiber pullout tests on CNT interfaces with polymer-derived ceramics that comprise elements of Si, C and O [16,17].

Our nanomechanical measurements clearly reveal that hBN is capable of forming a much stronger bonding interface with silica than graphene. To obtain mechanistic insights, we perform DFT calculations using the plane-wave-based Vienna Ab-initio Simulation Package (VASP) [18–20] to characterize the structural, as well as interfacial normal and shear adhesion properties of hBN and graphene on α-quartz (see *Computational Methods* in the Supplementary Materials). We consider three possible end-termination structures of α-quartz – silicon terminated (Si-), single oxygen terminated (Si-O-), and double oxygen terminated (Si-O_2-) – to represent the possible bonding structures formed between amorphous silica and the respective nanotubes.

Fig. 2 shows the quantum-mechanically relaxed structural configurations, along with contours of the corresponding electron localized function (ELF) along a cross-sectional cut about the x_1-x_3 plane depicting the probability (0 to 1) of finding an electron near another electron with the same spin. Our results suggest a clear dependence of the interfacial bonding characteristics on the type of end-termination structures of α-quartz, although the local bonding configurations and ELF values appear similar across the respective interfaces with graphene or hBN. Specifically, the low ELF values of ~0.2 across the interfaces of both Si- and O-terminated α-quartz with graphene or hBN suggest weak physisorption. Both graphene and hBN remain planar in these equilibrium structures, although we observe significant reconfiguration of the Si-O-terminated surface of α-quartz to form six-membered rings [10]. In contrast, the high ELF values of ~0.6 along the interfaces of Si-O_2-graphene and Si-O_2-hBN suggest strong chemisorption. In fact, our DFT calculations show the formation of two additional B-O bonds in our supercell with bond lengths of 1.481 and 1.482 Å across the interface of Si-O_2-hBN, which are close to the bond distance for tetrahedral B-O bond structures (1.475 Å) [21]. We also note the possible formation of an alternate stable Si-O_2-hBN structure comprising of a mixture of stronger B-O and weaker N-O bonds across the interface [15]. Similarly for Si-O_2-graphene, two C-O bonds with bond lengths of 1.470 and 1.484 Å are formed across the interface in our supercell, which fall within the range of C-O bond lengths in the normal (1.43 Å) and naturally stretched states (1.54 Å) [22]. As shown in Fig. 2, the formation of strong covalent bonds across these interfaces disrupts the planar structure of both hBN and graphene.

We obtain further insights into the interaction strength across the respective graphene-silica and hBN-silica interfaces through the interfacial separation distances δ (Table 1). Previous studies have used the equilibrium interfacial binding distance of $2.0 < \delta < 2.5$Å to denote chemisorption due to strong interactions, and $\delta > 3.0$ Å to denote physisorption associated with weak interactions [23]. Based on this simple criterion, both graphene and hBN are strongly chemisorbed on Si-O_2-terminated α-quartz (δ ~1.3 Å), but are weakly physisorbed on Si-terminated α-quartz (δ ~3.2 Å). While the bonding of graphene or hBN on Si-O-terminated α-quartz is also governed by physisorption, the smaller δ of ~2.9 Å suggests a much stronger interaction compared with that on Si-terminated α-quartz. These findings are also reflected in the adhesion energies of the respective structures (Table 1), which are computed by rigidly separating the relaxed configurations of the silica substrate and the atomic sheet by 10 Å and subtracting the energies of the isolated substrate and atomic sheet from the combined structure. In particular, we note the order of magnitude higher adhesion energies of the Si-O_2- versus both the Si-O- and Si-terminated structures, as well as the ~50% higher adhesion energy for Si-O- versus Si-terminated structures. In addition, we consistently observe stronger adhesion (higher adhesion energy with smaller δ) between the respective α-quartz structures and hBN versus graphene (Table 1), which can be alluded to the electrostatic interaction arising from dipole moment due to the electronegativity differences between B and N atoms in hBN.

Table 1
Adhesion energy and interfacial separation distance for graphene and hBN on α-quartz with different end-terminations.

VASP (DFT-D2)	Adhesion Energy (J/m^2)	Interfacial Separation Å
Si-graphene	0.1337	3.269
Si-O-graphene	0.2558	2.939
Si-O_2-graphene	3.8914	1.376
Si-hBN	0.1805	3.169
Si-O-hBN	0.2644	2.883
Si-O_2-hBN	4.4427	1.296

The interface between amorphous silica and CNT or BNNT has a mixture of Si-, Si-O-, and Si-O_2-terminated interfacial structures shown in Fig. 2. In the case of Si-O_2-terminated CNT or BNNT, the formation of clusters of covalent C-O, B-O, and potentially N-O bonds across the interface could prevent interfacial sliding and nanotube pullout. Along the weaker Si- and Si-O-terminated interfaces with the nanotube, however, interfacial sliding caused by shear will be the dominant failure mode. Accordingly, we construct the potential energy landscapes along the physisorbed Si- and Si-O-terminated interfaces with graphene and hBN to elucidate the barrier energies under interfacial sliding. To this end, we iteratively displace the graphene or hBN atomic sheet with respect to the silica substrate at 20 evenly-spaced intervals along each of the two in-plane vectors of each supercell (441 data points in total). After each translational displacement, we fix the in-plane coordinates of all atoms, while allowing them to relax in the out-of-plane direction (except for the atoms representing the bulk silica substrate), and compute the change in energy per unit interfacial area ΔG with respect to the energy minimized configuration.

As shown by the energy landscapes in Fig. 3a, the frictional force will depend on the direction of sliding. There are minimum energy pathways (MEPs) for interfacial sliding that weaves between energy minima. However, the nanotubes are unlikely to follow these MEPs during the dynamic and rapid pull-out process in our AFM experiments, especially given the rigidity of the SiO_2 substrates and the nanotubes. Instead, the stretching force along a fixed direction will force interfacial sliding to occur on a straight path during nanotube pull-out, and most sliding directions eventually cause the rolled graphene or h-BN to slide directly over the energy maxima at locations L1, L2, L3, and L6. We denote by arrows in Fig. 3a a sampling of possible straight pathways for interfacial sliding across one local minimum energy state (blue) to another (distributions of ΔG along each of these sliding pathways are shown in Figs. S4 and S5 of the Supplementary Materials). In the case of both Si- and Si-O-graphene, the critical barrier energies for interfacial sliding are ~0.02 J/m^2 along all three pathways, suggesting that the shear adhesion strength is largely independent of the sliding direction. Comparatively, the critical barrier energies for Si- and Si-O-hBN exhibit strong directional dependence varying from ~0.01 to ~0.03 J/m^2 across the three sliding paths.

The interaction of unterminated Si or O atoms in the silica substrate with only a single C atom type in graphene allows the sliding energy landscape to follow the 6-fold symmetry of graphene to provide near isotropic sliding response. The barrier peaks occur when the unterminated Si or O atoms reside at or near the top sites of the C atoms in graphene (L1, L2 in Fig. 3a). In contrast, the B and N atoms in hBN interact differently with the unterminated Si or O atoms, causing the sliding energy landscape to follow a 3-

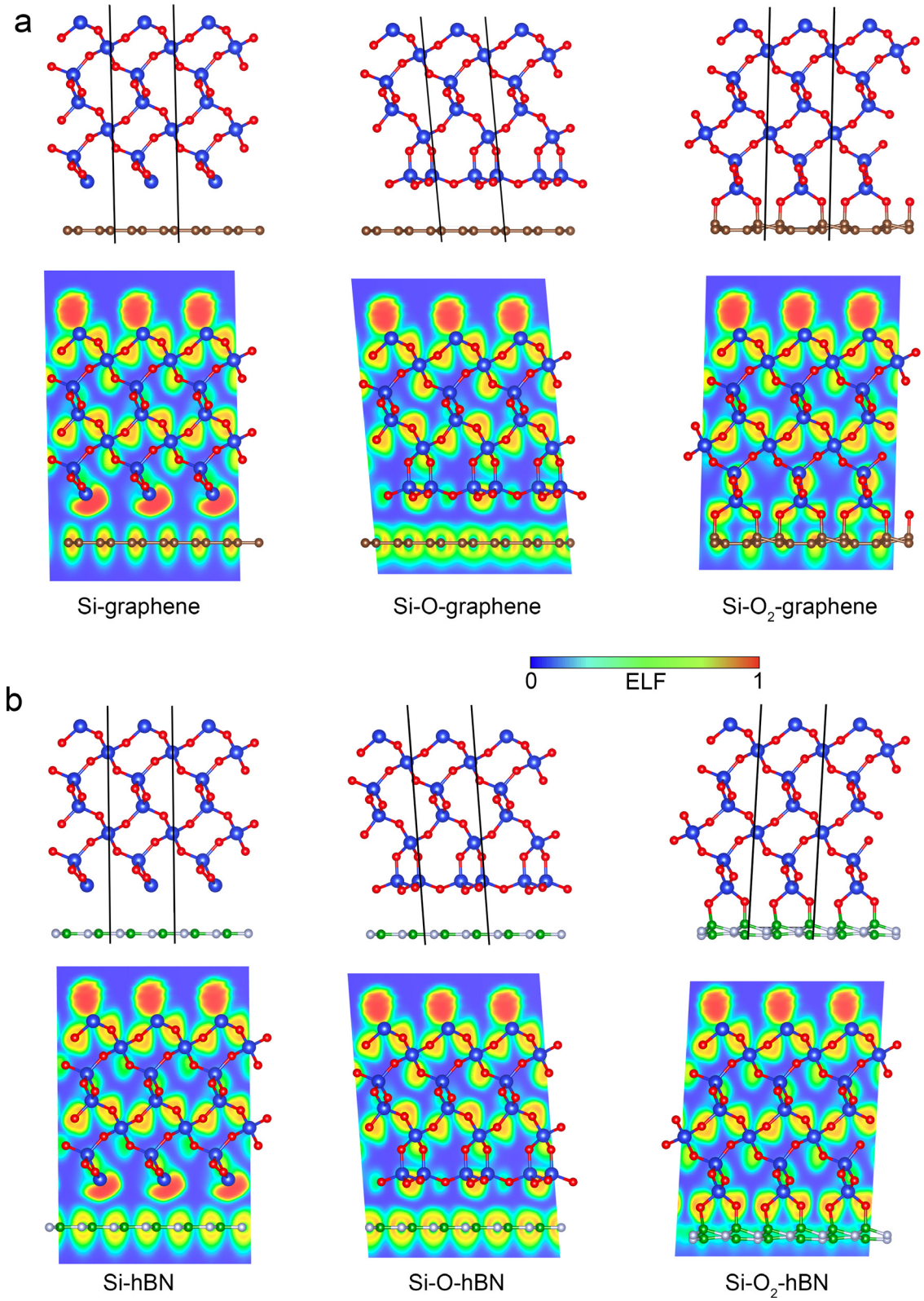

Fig. 2. Atomic configurations and ELF contours for graphene (**a**) and hBN (**b**) on α-quartz with different end-terminations. Atom colors: O (red), Si (blue), C (brown), B (green), and N (white) (For interpretation of the references to color in this figure legend, the reader is referred to the web version of this article.).

fold symmetry and exhibit significant path dependence. The peak barrier energies for Si-hBN and SiO-hBN occur along path 3 when unterminated Si or O atoms reside at the top sites of N atoms (L3, L6). Distinct minimum energy pathways within this anisotropic potential energy landscape are also observed along path 2 (crossing L4) for Si-hBN and along a zigzag path represented in-part by the initial segment of path 3 (crossing L5) for Si-O-hBN.

The adhesion energy is an order of magnitude larger than the barrier energy for interfacial sliding for the Si- and Si-O-terminated structures, suggesting that the sheet-substrate or tube-matrix in-

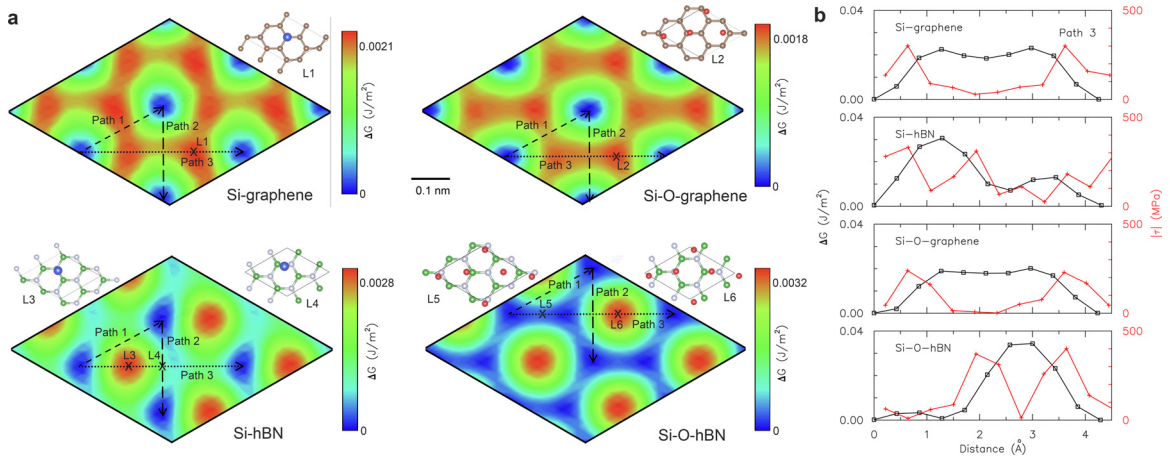

Fig. 3. Energy barriers for interfacial sliding. (**a**) Potential energy landscape for sliding of graphene and hBN on Si- and Si-O-terminated α-quartz, with close-up views of the relative positon of termination atoms with respect to the atomic sheet at the energy barrier locations labeled L1 to L6. Atom colors: O (red), Si (blue), C (brown), B (green), and N (white). (**b**) Sliding energy barriers ΔG (black) and interfacial shear stress $|\tau|$ (red) along the critical sliding path 3 in (**a**) (For interpretation of the references to color in this figure legend, the reader is referred to the web version of this article.).

terface is sufficiently strong to prevent decohesion and the formation of interfacial cracks during sliding. While interfacial sliding along semi-coherent or incoherent bimetal interfaces typically occurs through the movement of elastic non-crystalline dislocations following the MEP [24], we expect the peak barrier energies in the potential energy landscapes (along path 3 in Fig. 3a) to govern the shear-induced interfacial failure during pullout of nanotubes from amorphous silica matrices. This is because the high stiffness of the covalent Si-O, B-N, and C-C bonds in both the sheet and substrate, coupled with the low sliding barrier energies of ~ 0.04 J/m^2, does not readily permit the formation of interfacial dislocations (interfaceons). As aforementioned, interfacial sliding under the rapid nanotube pull-out process will be forced to trace out a straight line, with most sliding directions eventually crossing over the energy maxima, denoted by L1, L2, L3, and L6 in Fig. 3a. Such interfacial response can be represented by the change in potential energy ΔG along Path 3. As shown in Fig. 3b, we quantify the interfacial shear strength τ from the gradient of ΔG along these maximum sliding energy pathways (path 3), and show that τ is consistently higher for hBN versus graphene on both Si-terminated (331 MPa versus 301 MPa) and Si-O-terminated (401 MPa versus 240 MPa) α-quartz. This ultimately explains the $\sim$45% higher average IFSS for the BNNT-silica interface relative to the CNT-silica interface.

We remark that the binding interactions between silica and hBN or graphene tend to increase with the extent of uncoordinated O atoms along the free surface of silica, which transitions the interaction from weak physisorption (Si-, Si-O-) to strong chemisorption (Si-O_2-). In addition, the reaction of silica with water to form H- or OH- terminations will likely change the binding properties with the rolled 2D sheets [25]. The presence of structural defects in the nanotubes reportedly have a substantial influence on the nanotube-matrix interfacial strength [17]. These transitions in the interfacial properties explain the wide range of failure mechanisms, including interfacial sliding, matrix cracking, and nanotube fracture, previously reported for both CNT- and BNNT-reinforced silica composites [11–13].

In summary, we measure and compare for the first time the interfacial shear strength properties of graphene and hBN on amorphous silica through single-nanotube pullout force measurements and atomistic sliding energy landscape calculations. We show that hBN binds more strongly to silica than graphene, has higher interfacial shear strength, and exhibits stronger directional dependence in its sliding response. These results provide fundamental understanding of the nanoscale friction and interfacial shear properties, and have significant implications in the optimal design of atomistic interfacial structures to mitigate and ultimately control interfacial failure of ceramic nanocomposites, as well as graphene- or hBN-based atomic-scale devices.

Declaration of Competing Interest

The authors declare that they have no known competing financial interests or personal relationships that could have appeared to influence the work reported in this paper.

Acknowledgments

The authors acknowledge the support of the National Science Foundation under Grant Nos. NSF-CMMI 2009684, 2009134, and 2006127, as well as computational time provided by the Blue Waters sustained-petascale computing project, which is supported by the National Science Foundation (Awards No. OCI-0725070 and No. ACI-1238993) and the state of Illinois. Blue Waters is a joint effort of the University of Illinois at Urbana-Champaign and its National Center for Supercomputing Applications. C.M.D acknowledges fellowship support from the New York NASA Space Grant Consortium.

Supplementary materials

Supplementary material associated with this article can be found, in the online version, at doi:10.1016/j.scriptamat.2021.114413.

References

[1] A.L. Kitt, Z. Qi, S. Rémi, H.S. Park, A.K. Swan, B.B. Goldberg, Nano Lett. 13 (2013) 2605.
[2] G. Wang, Z. Dai, Y. Wang, P. Tan, L. Liu, Z. Xu, Y. Wei, R. Huang, Z. Zhang, Phys. Rev. Lett. 119 (2017) 036101.
[3] J.H. Hsu, S.H. Chang, Wear 266 (2009) 952.
[4] Y.J. Kang, J. Kang, K.J. Chang, Phys. Rev. B 78 (2008) 115404.
[5] M.Z. Hossain, Appl. Phys. Lett. 95 (2009) 143125.
[6] S.P. Koenig, N.G. Boddeti, M.L. Dunn, J.S. Bunch, Nat. Nanotechnol. 6 (2011) 543.
[7] M. Ishigami, J.H. Chen, W.G. Cullen, M.S. Fuhrer, E.D. Williams, Nano Lett. 7 (2007) 1643.
[8] M.F. Pantano, E. Iacob, A. Picciotto, B. Margesin, A. Centeno, A. Zurutuza, C. Galiotis, N.M. Pugno, G. Speranza, Carbon 148 (2019) 336.
[9] X.F. Fan, W.T. Zheng, V. Chihaia, Z.X. Shen, J.L. Kuo, J. Phys. Condens. Matter 24 (2012) 305004.
[10] W. Gao, P. Xiao, G. Henkelman, K.M. Liechti, R. Huang, J. Phys. D Appl. Phys. 47 (2014) 255301.

[11] A. Mukhopadhyay, B.T.T. Chu, M.L.H. Green, R.I. Todd, Acta Mater. 58 (2010) 2685.
[12] J. Cho, F. Inam, M.J. Reece, Z. Chlup, I. Dlouhy, M.S.P. Shaffer, A.R. Boccaccini, J. Mater. Sci. 46 (2011) 4770.
[13] P. Tatarko, S. Grasso, H. Porwal, Z. Chlup, R. Saggar, I. Dlouhý, M.J. Reece, J. Eur. Ceram. Soc. 34 (2014) 3339.
[14] X. Chen, M. Zheng, C. Park, C. Ke, Small 9 (2013) 3345.
[15] C. Yi, S. Bagchi, F. Gou, C.M. Dmuchowski, C. Park, C.C. Fay, H.B. Chew, C. Ke, Nanotechnology 30 (2019) 025706.
[16] A.J. Kessman, J. Zhang, S. Vasudevan, J. Lou, B.W. Sheldon, Adv. Mater. Interf. 2 (2015) 1400110.
[17] Y. Yang, C. Ramirez, X. Wang, Z. Guo, A. Tokranov, R. Zhao, I. Szlufarska, J. Lou, B.W. Sheldon, Carbon 115 (2017) 402.
[18] G. Kresse, J. Hafner, Phys. Rev. B 47 (1993) 558.
[19] G. Kresse, J. Furthmüller, Phys. Rev. B 54 (1996) 11169.
[20] G. Kresse, D. Joubert, Phys. Rev. B 59 (1999) 1758.
[21] W.H. Zachariasen, Acta Crystallogr. 16 (1963) 385.
[22] G. Gunbas, N. Hafezi, W.L. Sheppard, M.M. Olmstead, I.V. Stoyanova, F.S. Tham, M.P. Meyer, M. Mascal, Nat. Chem. 4 (2012) 1018.
[23] J. Tao, H. Tang, A. Patra, P. Bhattarai, J.P. Perdew, Phys. Rev. B 97 (2018) 165403.
[24] R. Li, H.B. Chew, Phil. Mag. 62 (2015) 1029.
[25] T. Zhu, J. Li, X. Lin, S. Yip, J. Mech. Phys. Solids 53 (2005) 1597.